![The University of Edinburgh logo]

Edinburgh Research Explorer

Fracture characterization of multi-layer wire mesh rubberized ferrocement composite slabs by means of acoustic emission

OPEN ACCESS

Fracture Characterization of Multi-Layer Wire Mesh Rubberized Ferrocement Composite Slabs by Means of Acoustic Emission

Arash Behnia[1*], Navid Ranjbar[2], Hwa Kian Chai[3]*, Aziz. I. Abdulla[4], Mahyar Masaeli[5]

[1]Discipline of Civil Engineering, School of Engineering, Monash University, Sunway campus

[2]Civil Engineering Department. Engineering Faculty, Shiraz University, Iran

[3]Civil and Environmental Engineering, School of Engineering, University of Edinburg, United Kingdom

[4]Department of Civil Engineering, Faculty of Engineering, University of Malaya, Malaysia

[5]Griffith School of Engineering, Griffith University, Gold Coast, Australia

Abstract

This study investigated the fracture behavior of multi-layer ferrocement composite slabs with partial replacement of tire rubber powder as filler utilizing Acoustic Emission (AE) technique for characterization. Ferrocement slab specimens prepared using normal-compact cement mortar, self-compact cement mortar, fly ash, and rubberized self-compact cement mortar –with varying steel mesh reinforcement layers– were statically loaded to failure. The inclusion of 10% rubber powder (by weight) was found capable of altering the failure mode of composite slabs from brittle to ductile with a slight reduction in the ultimate flexural strength. Fracture development of the specimens was closely monitored using AE for enhanced characterization. It is seemingly evident that the measured AE parameters could be effectively processed to distinguish different modes of fracture. The collected AE data was utilized to quantify stiffness reduction in the specimens due to progressive damage.

…………………………………………………………………………………………………….

Corresponding author: arash.behnia@monash.edu, hwakian.chai@ed.ac.uk

1. Introduction

Ferrocement structures are receiving a growing attention because of their high ductility, resistant to thermal cracking, easy fabrication and versatile installation (Ibrahim, 2011; Hago et al., 2005; Paul and Rama, 1978; ACI 549- 1R-93, 1993; Cheah and Ramli, 2012; Yerramala et al., 2013). These qualities enable successful use of ferrocement composites in numerous industries and applications, such as ship hulls, building construction and rehabilitation, sewerage pipelines, domes, and water tanks (Naaman, 2000).

Ferrocement is a hydraulic cement mortar with closely-spaced wire mesh reinforcement that could be made of a wide spectrum of materials including steel, polymer, synthetic woven fibres (Naaman, 2000). The closely-spaced reinforcement confines the cementitious matrix and enhances uniformity (ACI549- R97, 1997). In comparison with conventional isolated-bar reinforced concretes, ferrocement with multi-wire reinforcement provides larger surface contact energy. This, in turn, causes the matrix to gain a higher degree of energy absorption and, equally important, a higher modulus of rupture and elasticity. Ferrocement exhibits homogeneous isotropic mechanical and physical characteristics when reinforced multi-directionally. The high modulus of rupture of ferrocement composites combined with the excellent bonding between embedded internal mesh reinforcements and the surrounding cement mortar matrix contribute to their superb high tensile strength (Naaman, 1979; Kubaisy and Jumaat, 2005). It has been shown that the minimization of crack-width and subsequent performance enhancement in the ferrocement structures can be achieved by reducing the thickness of concrete or mortar cover of the elements (Kubaisy and Jumaat, 2005). However, thin ferrocement elements often suffer from difficulties during concrete vibration due to the congestion of reinforcement that could eventually lead to honeycombing and/or non-uniformity. Owing to its high flowability, self-compacting concrete (SCM) can, thus, be a suitable alternative to ordinary concrete in ferrocement production (Svec et al., 2014).

Full and partial replacement of fine aggregates by high energy-absorbent materials, such as rubber, could enhance toughness of the cementitious matrix as well as the mode of structural failure (Aitcin, 2000). The use of appropriate waste and by-product as a filler in ordinary or special concretes also enables production of durable, affordable and environmental friendly concrete (Su et al., 2015).

The global lavish and often reckless tire disposal poses an imminent environmental threat (Destroying the anti-leakage cover of the burial ground) as rubber is a non-degradable menace occupying significant surface and underground volumes in dumping yards (Oikonomou and Mavridou, 2009; Onuaguluchi and Panesar, 2014).

Incorporation of waste tires in concretes enables high tolerance to plastic deformation and superb fracture energy (Grinys et al., 2012). Benazzouk et al. (2007) reported that the use of rubber admixtures in concrete beams could reduce their brittleness whilst allowing greater plastic deformations. In addition, improvement in fatigue and impact resistance of tire rubber concretes and composites has been reported in numerous studies (e.g. Ganesan et al., 2013; Liu et al., 2012; Abdullah and Khatab 2014).

In view of this, ferrocement applications require maintaining a good balance between improving material ductility without compromising its strength. To this end, the induced plastic deformation capacity (strain rate) by introducing tire rubber into plain concrete is quite instrumental. Thus, replacing fine aggregate with rubber inclusions in normal and self-compacting concretes is believed to have a great potential. To the best of the authors' knowledge, research investigating rubberized multi-layered ferrocement slabs appears to be lacking.

To date, fracture behaviour of normal concrete ferrocement slabs are routinely investigated using experimental and analytical approaches (Cheah and Ramli, 2013). Nevertheless, considering the complexity of multi-layered composite ferrocement slabs, the sole implementation of those conventional methods might not suffice to fully capture the behavior of multi-layered ferrocement slabs. This could be more challenging when ferrocement slabs undergo an abrupt punching failure (Mansur et al., 2001). Therefore, utilizing a modern non-destructive technique like acoustic emission (AE) complements the current approaches with the superiority of online monitoring of material fractures.

There was an attempt to characterize rubberized concrete behaviour under three point bending using classical AE parameters which resulted merely in introducing a conventional damage index (Ho et al., 2012). The present study, however, has extended the use of AE technique to monitor and analyse the complex fracture behaviour, discriminate mode of failures, and provide an early warning system for failure of ferrocement composite slabs.

2. Acoustic Emission (AE) Technique

Acoustic emission is defined as the propagation of elastic waves due to the release of localized internal energy, such as micro-fracturing in an elastic material (Kaiser, 1950; RILEM TC 212-ACD, 2010; Grosse and Ohtsu, 2008; NDIS 2421, 2000; Aggelis et al., 2013; Farhidzadeh et al., 2013a; Behnia et al., 2014; Aggelis et al., 2013b; Soulioti et al., 2009; Farhidzadeh et al., 2013b). The source of AE activities are deformation processes in the structure, such as plastic deformation, crack expansion and other forms of material degradation. The procedure uses AE to detect the released strain energy generated from growing cracks using sensors (Behnia et al., 2014b). AE is capable of recording the damage process throughout the entire load history, which enables determination of the onset of fracture and tracking of the subsequent failure stages (Shiotani and Aggelis, 2007). Therefore, employing appropriate AE descriptors allows adequate estimation of the damage level and more insight into the nature of the failure. However, considering above mentioned advantages of AE, there is considerable potential to utilize AE in material behaviour studies other than monitoring and assessing damage levels in composite materials.

3. Materials and samples preparation
3.1. Materials
a. Cement

Locally sourced ASTM (American Society Testing Material) Type I Ordinary Portland Cement (PC) was used in this study as the key binder material.

b. Fly ash

It is imperative to enhance the amount of 'pastry' (Pate-like material) in the self-compacting mortar (SCM) because it is an agent that holds the aggregates. This becomes more critical when rubber tires powder is added in the mortar. Low calcium fly ash (FA - class F) supplied by Lafarge Malayan Cement Bhd, Malaysia, was used for this purpose. Due to the round particle shape and high silica content, incorporation of fly ash has the potential to reduce the water demand and enhance the flowability of the fresh matrix (Ranjbar et al., 2014). Phenom ProX scanning electron microscopy (SEM) was used to observe the interfacial bond of the rubber particles and matrix. The chemical composition of used FA is shown in Table 1.

c. Fine aggregate

Locally available river sand with grading in accordance with the limit values specified by British Standard (BS882-1992) was used for the mortar mixes. The sand was washed prior to mixing to remove the natural silt and clay in the raw stockpile.

d. Rubber

Locally provided tire rubber particles with 200 μm average particle size and density of 1.15 g.cm^{-3} have been used in the rubberized self-compacting mortar (RSCM) mixtures. The chemical composition and physical properties of rubber are presented in Table 3.

e. Internal welded wire mesh

A total of four, six, and eight layers of welded galvanized steel square mesh with a wire diameter of 1 mm and spacing of 13 mm were provided as internal reinforcement for the fabricated ferrocement slab. The mesh was tested in the laboratory according to the design guide for construction and repair of ferrocement reported by the ACI Committee 549 (1993). The yield strength of the wire mesh was determined to be 300 MPa with an average ultimate strength of about 335 MPa.

3.2. Samples preparation and mortar properties

a. Casting and sample preparation

Open top and bottom steel moulds with dimensions of 500 mm x 500 mm x 30 mm were used. A thin layer of mortar was initially poured to warrant the desired cover thickness prior to the placement of the wire mesh in the slab specimen. The mortar was evenly spread into the reinforcement network. The finishing step was performed by levelling a thin layer of mortar to ensure a smooth top surface. The specimens were left in room temperature for 24 hours to set after casting.

Twenty one samples in the form of twelve specimens for three different types of mortar were prepared for this study: normal cement mortar (NM), self-compact mortar (SCM), and rubberized self-compact mortar (RSCM). The used mix design is presented in Table 2. To produce the SCM, all the aggregates were first mixed in a dry state. Next, fly ash (FA) and cement were added. After a homogeneous dry mixture was achieved, 80% of the design water content by volume was added. Chemical admixture separately dissolved in the remaining 20% water content was finally added to the mixture. The mixing process continued until the mixture was consistent in self-compactability.

5

b. Fresh and hardened properties of mortar

Table 4 presents key fresh and hardened properties of normal and self-compacted mortars. According to the criteria provided by Ranjbar et al. (2016a), it is evident that the used self-compact mortars meet the reported standard values in terms of flowability, passing ability (mini slump flow- J ring), workability and level of segregation. The inclusion of rubber particles, however, reduces slump flow, with the reduction increased with rubber content. It is, thus, anticipated that the addition of rubber decreased mini slump flow and mini J ring spread, while increased the V funnel test time. Nevertheless, the inclusions of sufficient portion of superplasticizer and FA have maintained the self-compacting mortars fresh properties within the acceptable limits (EFNARC). Partial replacement of Portland cement with the lower specific gravity substitute (FA) has given rise to the smaller mortar density (Table 1). In addition, the readily roll over action between the spherical FA particles minimizes interparticle friction, which yields higher flowability.

4. Test set up and Instrumentation
4.1. Test set up

The testing machine and schematic detail of the test procedure is given in Figure 1. A total of twelve slab specimens were prepared with geometrical and material variations given in Table 2. For each type of mortar (NM, SCM, SCMR5, and SCMR10), specimens with four-, six-, and eight- mesh layers were prepared. To study the behaviour of different specimens, a concentrated monotonic loading through a steel disc was applied at the centre of the specimen.

4.2. Acoustic emission instrumentation

The AE measurement system adopted in the experimental study consisted of PCI-2 data acquisition boards (by Mistras Group Inc) that accommodate a total of six AE sensors and a Windows-based AE data operation program known as AEwin. The AE sensors used have a resonant excitation frequency of 60 kHz (R6I). A total of six sensors were mounted by specific type of elastomer dry-couplant on the specimens as shown in Figure 1. In the measurements, the sampling rate for AE monitoring was set to 2 MHz with the pre-trigger set to 250.000 μs. The hit definition time (HDT), hit lockout time (HLT), and wave velocity were configured as 200 μs, 300 μs and 3900 m/s, respectively. To eliminate electrical and mechanical noise, the threshold level of acquisition was set at 50 dB. During the post processing of acquired AE data,

further de-noising processes was performed, following the procedures presented by Behnia et al. (2015)

5. Results and discussion

5.1. Mechanical behaviour

The load versus central deflection curves as well as crack and failure patterns for the ferrocement slabs have been used to analyse and classify the modes of fracture and types of failure. Figure 2 and Table 5 present the load-deflection curves, Ib-value results, and the summary of specimens' mode of failure. Detailed discussion on Ib-value is provided later in section 5.3.3.

From Figure 2 and test observations, it can be concluded that normal mortar specimens of four mesh layers failed in the flexural mode (The large load-deformation and large post peak deformation), while increasing the mesh volume fraction (number of layers) changed the failure mode to punching failure (The high peak load but small post peak deformation). As can be observed in Figures 2a-d, the wire mesh resists tensile load in tension zone of the slab. When the number of mesh layers were increased from four to six and ultimately eight, the specific surface, mesh fraction volume, and the confinement of the cementitious matrix increased resulting in a larger flexural strength. For example, from Figure 2a and Table 5 it can be observed that upon increasing the number of mesh layers from four (NM4) to six and eight, the ultimate load and flexural strength improved by up to 63% and 109% for NM6 and NM8, respectively. However, with two or more additional layers of wire meshes, the mode of failure for normal mortars changed from flexural to punching shear. This was manifested in the sudden formation of a hole on the top surface of the slab and the truncated large diameter failure cone on the bottom face. In addition, considering the toughness values (i.e. energy absorption) presented in Table 5, it was found that for the case of normal mortar, toughness was considerably improved by increasing the volume fraction of wire meshes. Ductility ratio, calculated as the ratio between the ultimate deflection and the deflection at the first visible crack, was proposed as a measure of specimen ductility. Despite its total lower energy absorption, NM4 was slightly more ductile than NM6 and NM8.

Replacing normal mortar with self-compacting mortar resulted in a considerable increase in the ultimate load and flexural strength. Compared to NM4, SC4LR0 ultimate failure load and flexural strength were considerably increased to approximately 46% and 44%, respectively. It is noteworthy that replacing normal cement mortar with self-compacting mortar for the four-layer wire mesh configuration approximately yielded 46% and 49% increase in toughness until failure and total toughness, respectively. Interestingly, the ultimate deflection for SC4LR0 was increased up to 16 % compared to NM4, whereas the ductility ratio declined by approximately 32%. This observation was associated with noted differences the in tensile strength between these two mortars. Although SC4LR0 displayed larger deflection than NM4, tensile strength for normal cement mortar was about 47 % lower than that of the self-compacting mortar. On the other hand, the first visible crack took place when the tensile strain in the extreme lower fibre of the slab exceeded the ultimate tensile strength of the mortar. Hence, self-compacting mortar with higher tensile strength and strain underwent the first crack, comparatively, after the normal cement mortar. Although the replacement of normal mortar with self-compact mortar caused slight changes in mode of failure, similar to normal mortar specimens with six and eight layers, the dominant failure mode of SC6L0 and SC8L0 was in punching but with emergence of flexural cracks prior to punching failure in these specimens.

In general, inclusion of rubber in self-compact mortars decreased ultimate load and flexural strength. However, inclusion of 5% and 10% of rubber in self-compacting mortars exhibit different slab behaviours. At 5% rubber replacement a slight decrease in flexural strength and energy absorption were noted, whereas in all other cases ductility ratio was increased relative to the self-compact mortar without rubber. In addition, there was no significant change caused in modes of failure. On the other hand, the 10% rubber inclusion caused significant changes in flexural strength and slab behaviour. Compared to self-compact mortar without rubber, the addition of 10% of rubber significantly decreased the ultimate load and flexural strength but compensated this with higher energy absorption and ductility ratio. For example, flexural strength for SC4LR10 in comparison with SC4LR0 declined about 12%, whereas the failure deflection and ductility ratio were considerably increased to 26% and 36%, respectively. Moreover, inclusion of 10% rubber effectively changed the failure modes to flexural (SCR10). Therefore, although with inclusion 10% rubber the flexural strength was reduced, yet the tensile strain at ultimate failure increased (e.g. SC8LR10).

Enhancement mechanism of the mechanical properties of composite materials is primarily governed by the dispersion uniformity of the inert particles and their interfacial contact strength with the binder matrix (Ranjbar et al., 2016b). Uniform dispersion of particles is controlled by external factors including proper mixing, volume of incorporation and vibration condition of the fresh matrix. However, the interfacial bond between the two phases is dependent on intrinsic characteristics of the inert material, chiefly: surface roughness and degree of hydrophobicity (Ranjbar et al., 2016c). Rubber particles have a hydrophobic nature driven by non-polarity. This character is responsible for repelling cement paste in fresh state, which subsequently forms air entrapment at the particle surfaces and increase porosity at the macro level. Unsurprisingly, this weakens interfacial bonding between cement and rubber (filler) – the key reason behind the reduction of flexural strength of the matrix. From a morphology perspective, the SEM image of the mixture revealed modest corrugation of the rubber surface with a higher degree of uniformity along the smoother surface compared to the mortar matrix. In addition, the efficiency of the bond in this composite highly depends on the quality of bond between rubber and matrix, since, ferrocement is a water-based matrix and the bond quality is governed by wettability of rubber by water, therefore, the low wettability of rubber resulted in poor bond adhesion (Ranjbar et al. 2016b). Chemistry of the interaction also adds to the evident weak bonding. The zinc stearate in rubber migrates and spreads along the rubber surface creating water-repellent soap layer, and thus, adds to the mechanically-induced weak bonding between rubber and ferrocement (Fernando et al., 2011). The poor adhesion between the two phases and trapped air bubbles around the rubber particles are both captured in the SEM images (Figure 3).

The foregoing observations collectively promote weak bonding between rubber and mortar. Therefore, with sufficient rubber volume fraction the reduction of flexural and compressive strength of the rubberized mortars becomes inevitable. Noting that the observed cracks were usually formed and propagated along the rubber-cement interfacial transition zone (ITZ).

The inclusion of small amount of rubber may not significantly improve toughness of the mixture. However, at a considerable rubber inclusion in the matrix enhancement of energy absorption capacity of the composite is observed. This can be attributed to entanglement of rubber and interlock between rubber and aggregates. This phenomenon causes rubber acts as a hook and resists some loads before pull-out. The entanglement in rubber is due to higher Poisson ratio of rubber which is nearly 0.5, whereas mortar/sand Poisson ratio is between 0.2-0.4. Therefore, rubber comparatively enjoys a higher level of elasticity; therefore, it could delay and suppress initial crack growth in the matrix (Edward and Viglis, 1988).

5.2. Generalized behaviour under mechanical loading

Through test observations, analysis of mechanical results and as depicted in Figure 4, the behaviour of the specimens can generally be categorized into two principal failure modes: flexural and punching.

From the shear failure patterns shown in Figures 2 and 4a, an abrupt decrease in loading occurred post peak, forming a vertical drop in the load-deflection curve. As a typical behaviour, there was a semi-linear relationship between loading and deflection until flexural cracking, which occurred in the centre of the loading path. After cracking, a noticeable reduction in stiffness could be noted. As the load increased, new cracks were formed and the existing cracks appear to propagate radially. The load-deflection curve slope (stiffness) gradually decreased until the final punching failure – highlighted by a sudden drop in the applied load. At this moment, punching shear pattern was quite obvious, indicated by the formation of a "hole" on the top face of the specimen. Crack traces of a truncated failure cone were merely noted with a larger diameter on the bottom face of the specimen.

When most of the reinforcement yielded prior to failure and the slabs subsequently underwent large deflection, the dominant failure mode was evidently flexural. The flexural failure as illustrated in Figures 2 and 4b, could be characterized as a smooth decline of the carrying load accompanied by a progressive increase in deflection. In general, when ferrocement slabs are subjected to flexural load, the development of fracture behaviour can be attributed to three stages: elastic stage/pre-cracking stage, elasto-plastic stage/multiple cracking stage, and plastic stage/post-cracking stage (Cheah and Ramli, 2012). First, a homogenous elastic material until the first visible crack occurs. Second, multiple cracks are formed until the onset of reinforcement yielding. At this stage the length and number of cracks increase, and simultaneously the cracks width does not seem to increase. Finally, yielding of reinforcement together with crack-widening are continued until ultimate failure. In some cases where a second peak was usually observed from the load-deflection curve, flexural punching failure was found. In such cases, the continuity between the punched area and either portion of the slab was maintained through the wire mesh reinforcement, giving rise to the second peak in the load-deflection curve after punching. The occurrence of the second peak could be explained by the development of a tensile membrane action given by the wire mesh.

To sum up, based on load-deflection curve, strain in reinforcement, and the emergences and propagation of cracks during the experiment, the fracture of slabs can best be classified as a multi-staged process. This shall be discussed in the next section.

5.3. Acoustic emission (AE) monitoring

5.3.1. AE parametric analysis and material properties correlation

Figure 5 depicts the variation of cumulative AE hits along the applied loading. Limited AE activity can be noticed in the elastic loading region prior to occurrence of the first crack. Upon the appearance of macro cracks in the slab, a sudden increase in AE hits is recorded. The rate of cumulative AE hits progressively increases thereafter until the monotonic loading approached its ultimate value. At fracture of the slab (maximum load capacity), the cumulative AE hits continue to increase at a lower rate than the previous stage. However, information obtained by cumulative AE hits analysis merely provided a general idea of the failure progress. Therefore, in order to characterize the material properties and behavior of different slabs, analysing the actual rate of AE hits shall be used as an informative analysis.

Table 5 addresses punching and flexure, the principal modes of failure induced by the influence of material properties and reinforcement configuration. Figure 6 presents typical samples of AE hit rate for punching and failure modes against load.

The first type of slab (e.g. NM6) failed in a punching mode which showed a membrane action. For these slabs, the fracture process starts with micro-cracking stage (I), designating the so-called pre-cracking or elastic stage, with AE activity level considerably lower than those in the subsequent stages (Figure 6a). Upon the emergence of the first macro-crack/flexural crack at center of the bottom face of slab, distinguished by the reduction in the load-deflection slope, a sudden increase in the AE hit rate was registered. This stage (II) –demarking the elastic behaviour after the first nonlinearity– is called post-cracking/multiple cracking or elasto-plastic cracking. The AE rate remained moderate due to either propagation of existing cracks or the occurrence of new cracks until the peak load at which the punching failure is apparently more pronounced. Punching failure coincided with the main shock of the AE hits rate identified by the maximum rate of AE hits. The subsequent considerable drop in AE hits rate observed in the post-punching stage (III) appears to be commensurate with the significant plunge in loading. In this stage, the tensile reinforcements started to yield. Most AE hits in this stage can be attributed to the crack widening and yielding tensile reinforcement in the form of membrane action within the slab. Hence, yielding of reinforcement results in a low population of AE activity with a higher amplitude compared to the previous stages (Behnia et al., 2014a).

The second type of slabs (e.g. SC4LR5) exhibited flexural failure (Figure 6b). Stages I and II of fracture process are similar to those observed for the first type of slab. At the end of elasto-plastic stage, the slope of the load-deflection curve experiences further decrease gradually transforming the behavior to plastic or post-yielding stage (III) until peak load. The AE hit rate in the post-yielding stage was characterized by a moderate decreasing trend until the peak load (Figure 6b). This phenomenon may be caused by yielding of the reinforcement that drives a reduction in AE signal emission. In the post-peak stage, the tensile reinforcements tend to tear out of the concrete accompanied by bond failure (debonding). This could ultimately result in the fracture of meshing around the centre of loading in the truncated zone. The observed main shock of AE is indicative of the considerable increase in AE activity for the initial period of this stage. This phenomenon may be caused by the emission of AE signals resulted from bonding failure between reinforcement and concrete or reinforcement tearing.

It the next stage effect of rubber inclusion on the variation of AE hit rates is closely investigated. Driven by its high ductility, inclusion of 10% rubber could completely change the material behaviour by switching the mode of failure from punching to flexural. These transformational changes to the material behavior are directly captured by AE hit rates. For instance, Figure 7 illustrates the trend of AE hit rate for SC6LR10 and SC8lR10. For these cases the first stage still resembles the observed response of the other slab types. Low and moderate AE activity was registered in the pre-cracking stage, whereas the highest AE activity occurred in the second stage (multiple cracking/post cracking). However, by comparing Figures 6 and 7, it can be realized that 10% rubber inclusion could significantly decrease the AE hit rate. This is directly governed by the ductility of rubberized slabs, as ductility increased the AE activity decreased.

As depicted in Figure 7 by the occurrence of the first macro-crack (Stage I), a significant increase was observed in the AE hits rate. It is notable that the main shock of AE hits rate took place in the multiple cracking stage (Stage III), occurring before the peak load. However, the incremental trend of occurrence of AE hits in this stage (II) is considerably higher than other stages. The main reason for this phenomenon may be attributed to the properties of the rubberized mortar. In this stage, local fractions/debonding and dislocations occur along rubber/binder interface due to the weak interfacial contact properties. Hence, the number of cracks and AE hits could be significantly increased. Starting from the yielding stage, the AE

hits decreased until the peak load. This is followed by widening of the main cracks, extended along the length of slabs, until the end of the fracture process. Therefore, the number of generated AE hits with higher amplitude or energy continues to diminish.

An innovative attempt was made to correlate the number of AE hits with slabs' stiffness variation. As an example, Figure 8 shows the occurrence of AE hits against time NM6. It was observed that there is a sudden increase in the number of AE hits with a significant drop in the stiffness curve near the ultimate peak load. In order to attain quantitative information for the failure process, normalized cumulated AE hits were plotted against the loss of slabs' stiffness with loading. For example, Figure 9 shows the variation of loss of stiffness versus the normalized cumulative AE hits for NM6, SC4LR0, and SC8LR5.

It can be inferred that the increase in number of AE hits was accompanied by the loss of stiffness. Interestingly, it was found that a general Gaussian distribution could be developed to estimate the loss of stiffness relative to the number of cumulative hits for all tested slabs. Therefore, the following simple Gaussian model with a single one term is proposed to estimate the loss of stiffness in online AE monitoring:

$$F(x) = a_1 * e^{\left(-\left(\left(\frac{x-b_1}{c_1}\right)^2\right)\right)} \tag{1}$$

where x is variable of accumulated AE hits and a, b, and c are constant obtained from the test data. It was demonstrated that this Gaussian distribution with almost 95% confidence level is valid. The detail of error and R-square values are summarized in Table 6.

5.3.2. AE technique for structural behavior analysis

AE technique can evaluate the condition of structural elements by monitoring active cracks using transducers mounted on the specimen. The transducers facilitate recording the transient response induced by cracking events. Parameters, such as event and damage location, nature of damage, and severity of damage can be addressed by AE analysis. The obtained information from sensors is associated with the effect of fracture of material on the signal waveforms (Aggelis et al., 2013a). Therefore, differences in emitted signals could be attributed to individual failure mechanisms. There are several AE parameters that have the potential to grasp the fracture process signature. Thus far, average frequency and RA (rise time/amplitude) were used to discern tensile cracking from shear cracking during the fracture process (Aggelis, 2013a; Aggelis, 2013b; Behnia, 2015). The sensitivity of RA and average frequency (AF) for flexural and punching mechanisms are examined in this study. NM6 slabs are selected as a

sample for illustration purposes. Figure 10 shows the trend of variation in RA and AF, respectively. Interestingly, distinct effects of the fracture progress on RA and AF could be observed. The first visible crack on the surface triggered by flexure is characterized by RA surge and a significant drop in AF. The simultaneous increasing RA and decreasing AF trends persist until the ultimate load capacity with paramount RA peak in and considerable AF drop registered at failure. RA and AF can be appreciably affected by the nature of source of the imposed structural damage.

In comparison with flexural cracking, punching could cause a higher level of increase and decrease in RA and AF, respectively (Figure 11). The RA value controlled by the first part of waveform shifted to a higher value as the structural damage changed from flexural to punching (Figure 11a). It can be seen that the average trend for SC4LR0 with flexural failure was lower than those relating to NM6 and NM8 with punching failure. This phenomenon can be attributed to the wave modes which would be excited by different type of cracks or damages. Flexural failure might be accompanied by tensile cracks resulting in a transient or short-term burst of volumetric change inside the material. This type of volumetric change converts the released energy to a longitudinal or dilatational wave (p-wave). Most excited pulses consist of longitudinal waves with larger amplitude and, subsequently, they travel faster than other types of waves having shorter rise time signals (Behnia et al., 2014b).

On the other hand, punching failure is principally accompanied by shear cracks through which most energy would be transmitted to distortional shear waves (s- wave). Excited longitudinal waves, however, could still be active. However, it is known that a shear wave is the wave in which the oscillations are occurring perpendicular to the direction of the wave propagation, and consequently the wave velocity is slower than p-wave. Thus, most of energy transmitted through the s-wave arrives after the first p-wave arrivals leading to longer rise time. The s-wave, yet, embraces a larger amount of energy than the P-wave (s-wave amplitude > p-wave amplitude). Holding this wave propagation perspective, punching failure shows a higher RA value than flexural failure. Figure 11b depicts AF curves for flexural and punching failure specimens. Generally, AF was shifted to a lower value as damage was altered from flexural to punching. This observation is in good agreement with the work by Shah and Li (1994) indicating that the p-wave has higher frequency than the s-wave. Therefore, flexural failure shows higher frequency than punching failure when flexural failure is dominant.

Failure type identification was furnished via close investigation of collected RA and AF data for different samples. Figure 12 depicts AF and RA data incorporated in to a single graph to allow discerning flexural failure from punching failure. The classification of failure types was performed successfully so that the results presented in the Figure 12 are in agreement with failure types presented earlier in Table 5. To separate flexural and punching failure, predefined diagonal lines in the figures were defined based on results presented in the Japan Construction Material Standards (JCSM, 2003). It should be noted that this predefined diagonal line might be a general separation line so that precise clustering can be obtained through classification methods for which some innovative techniques were developed by some researches (Farhidzadeh et al., 2014). However, as depicted in Figure 12a for the flexural failure case (SC4LR0) data located above the diagonal line and punching failure cases, NM6 and NM8, some parts of data were positioned below the diagonal line. In another example, Figure 12b is comparing the failure behaviour for different types of ferrocement material with 8 layers of wire mesh. It was observed that the transition of punching failure (NM8, SC8LR5) to flexural (C8LR10) was successfully captured. It is noteworthy that some data fall above the diagonal line for those cases of punching failure. It is justified simply by the concept of fracture process. Fracture process in this slab starts by micro-cracking and then continues by tensile macro-cracking of the matrix which generates tensile or flexural cracking signatures.

5.3.3. Early warning failure system

Considering the overall behaviour of ferrocement slabs, punching failure could abruptly occur in some cases shown in earlier sections. However, adequate employing of AE parameters could possibility serve as an early warning system. It is known that macro-cracks produce a higher amplitude than micro-cracks (Aggelis et al., 2011). Due to the occurrence of macro-cracking events, a high amount of the elastic energy can be released resulting in high amplitude events. Therefore, it is reasonable to use amplitude distribution during the fracture so that the damage progress can be predicted. Conseuently, the "Ib-value", the ratio of weak to strong events, can be utilized to gauge structural damage as follows (Shiotani et al., 1994):

$$Ib = \frac{[log\ N\ (\mu - \alpha_1.\sigma) - log\ N\ ((\mu + \alpha_2.\sigma)]}{(\alpha_1 + \alpha_2)} \qquad (2)$$

Where μ is the mean amplitude, σ the standard deviation, and α_1 and α_2 are user-defined constants which represent coefficients of lower and upper limits of the amplitude range to yield

a straight line. With preceding explanations, micro-cracking causes a relatively high Ib-value, which is the absolute value of the slope of the cumulative amplitude distribution, whereas macro-cracking results in relatively low Ib-values. The detail of the above formula can be found in reference [35]. However, the average calculated Ib-value is superimposed in the load-deflection curve presented in Figure 2. In general, there were two sizeable drops in Ib-value trends. The first drop occurred simultaneously with the formation of the macro-cracks and the second and more significant drop occurred much earlier than the peak load. However, although the main drop in Ib-value results took place much earlier than the peak load, the Ib-value decreased in specimens with punching failure earlier than specimens undergoing flexural failure. The main drop in Ib-value occurred at 85% of ultimate load for NM4, whereas this drop ranged from 65-73% of ultimate loading in specimens with punching failure. It was also noted that the Ib-value at fracture ranged from 0.06 to 0.09. The drop can be attributed to the macro-crack formation and localization and can, thus, serve as a measure for early warning failure.

6. Conclusions

Twelve ferrocement multi-layered composite slabs, including normal cement, self-compact mortar, and rubberized self-compact mortars with varying mesh layers, were subjected to concentrated loading. Rubber powder of tires was used as a potential by-product replacement in self-compact mortars. Acoustic emission technique was incorporated into the mechanical macro- and micro-structure analysis to monitor the fracture initiation and propagation in ferrocement composite slabs. The following summarizes the key findings of the study:

1) Rubber powder can be used in self-compact mortar partially in lieu of filler with a potential slight reduction in the ultimate load capacity of slabs. At 10% inclusion, however, rubber powder enhanced ductility that triggered a sharp change in failure mode, from punching to flexure. In addition, an increase in the number of wire meshes has increased the flexural strength of slabs resulting in punching failure.

2) The acoustic emission technique was successfully employed to characterize the fracture behavior of slabs regardless of mortar type/properties. AE hits rate variation could differentiate various stages of fracture. The structural behaviour of slabs and types of failure, punching and flexural, were characterized by the aid of AE parameters as a source discrimination system.

3) AE hits can be correlated with the reduction in structural stiffness using Gaussian distribution. AE hits amplitude distribution (Ib-value) could serve as an early warning failure system.

Reference

Abdullah, A.I., Khatab, H.R., 2014. Behavior of Multilayer Composite Ferrocement Slabs with Intermediate Rubberized Cement Mortar Layer. AJSE. 39 (8), 5929-5941.

ACI Committee 549, 1997. State-of-the-art report on ferrocement. ACI 549- R97, in Manual of Concrete Practice, ACI. American Concrete Institute

ACI 549.1R 93, 1993. Guide for the design, construction and repair of ferrocement. Manual of Concrete Practice. Michigan: American Concrete Institute.

Aggelis, D.G., Mpalaskas, A.C., Matikas, T.E., 2013. Investigation of different fracture modes in cement-based materials by acoustic emission. Cement Concrete Res. 48, 1-8.

Aggelis, D.G., Soulioti, D.V., Gatselou, E.A., Barkoula, N.M., Matikas, T.E., 2013. Monitoring of the mechanical behavior of concrete with chemically treated steel fibers by acoustic emission. Construct Build Mater. 48, 1255–1260.

Aggelis, D.G., Soulioti, D.V., Sapouridis, N., Barkoula, N.M., Paipetis, A.S., Matikas, T.E., 2011. Acoustic emission characterization of the fracture process in fibre reinforced concrete. Construct Build Mater. 25, 4126-4123.

Aitcin, P.C., 2000. Cements of yesterday and today concrete of tomorrow. Cement Concrete Res. 30, 1349-1359.

Behnia, A., Chai, H.K,. Ranjbar, N., Jumaat, M.Z., 2016. Damage detection of SFRC concrete beams subjected to pure torsion by integrating acoustic emission and Weibull damage function. Struct Control & Health Monit. 23 (1); 53-68.

Behnia, A., Chai, H.K., Shiotani, T., 2014a. Advanced structural health monitoring of concrete structures by means of acoustic emission. Construct Build Mater. 65, 282-302.

Behnia, A., Chai, H.K., Yorikawa, M., Momoki, S., Terazawa, M., Shiotani, T., 2014b Integrated non-destructive assessment of concrete structures under flexure by acoustic emission and travel time tomography. Construct Build Mater. 67, 202-2015.

Benazzouk, A., Douzane, O., Langlet, T., Mezreb, K., Roucoult, J.M., Queneudec, M., 2007. Physicomechanical properties and water absorption of cement composite containing shredded rubber wastes, Cem Concr Compos. 29(10), 732-740.

BSI. BS 882, 1992. Specification for aggregates from natural sources for concrete. British Standards Institution. London.

Cheah, C.B., Ramli, M., 2012. Load capacity and crack development characteristics of HCWA–DSF high strength mortar ferrocement panels in flexure. Construct Build Mater. 36, 348-357.

Edward, S.F., Vilgis, T., 1988. The effect of entanglements in rubber elasticity, Polymer. 27 (4), 483-492.

EFNARC, Test methods—Annex D, 2002. Specifications and Guidelines for Self-Compacting Concrete, web site: http://www.efnarc.org, Farnham, UK, 21–24.

Farhidzadeh, A., Salamone, S., Singla, P., 2013a. A Probabilistic Approach for Damage Identification and Crack Mode Classification in Reinforced Concrete Structures, J Intel Mat Syst Str. 24 (14), 1722-1735.

Farhidzadeh, A. C. Mpalaskas, T. E. Matikas, H. Farhidzadeh, D. Aggelis, (2014), Fracture mode identification in cementitious material using supervised pattern recognition of acoustic emission features, Construction and Building Materials, 67: 129-138.

Farhidzadeh, A., Salamone, S., Luna, B., Whittaker, A., 2013b. Acoustic emission monitoring of a reinforced concrete shear wall by b-value–based outlier analysis, Structural Health Monitoring, 12 (1): 3-13.

Fernando, P., Nilomar, Z., Tiago, L., 2011. Adriano B. Concrete made with recycled tire rubber effect: Effect of alkaline activation and silica fume addition. J Clean Prod. 19, 757-763.

Ganesan, N., Raj, B.J., Shashikala, A.P., 2013. Flexural fatigue behavior of self-compacting rubberized concrete. Construct Build Mater. 44, 7-14.

Grosse, C.U., Ohtsu, M., 2008. Acoustic emission testing. Springer, Heidelberg.

Grinys, A., Sivilevicius, H., Dauksys, M., 2012. Tyre rubber additives effect on concrete mixture strength, J. Civ. Eng. Manag. 18(3), 393-401.

Hago, A.W., Al-Jabri, K.S., Alnuaimi, A.S., Al-Moqbali, H., Al-Kubaisy, M.A., 2005. Ultimate and service behavior of ferrocement roof slab panels. Construct Build Mater .19, 31–37.

Ho, A.C., Turatsinze, A., Hameed, R., Vu, A.C., 2012. Effects of rubber aggregates from grinded used tyres on the concrete. J Clean Prod, 23: 209-215.

Ibrahim, H.M., 2011. Experimental investigation of ultimate capacity of wired mesh-reinforced cementitious slabs. Construct Build Mater. 25, 251–259.

JCMS-IIIB5706. 2003. Japan Construction Material Standards. Monitoring Method for Active Cracks in Concrete by Acoustic Emission. Japan: The Federation of Construction Material Industries.

Kaiser J: 'Untersuchung über das Auftreten von Geräuschen beim Zugversuch', Dr.-Ing. Dissertation, Fakultät für Maschinenwesen und Elektrotechnik der Technischen Universität München (TUM); 15.2.1950.

Kubaisy, A.M., Jumaat, M.Z., 2005. Crack control of reinforced concrete members using ferrocement tension zone cover. J Ferrocement. 35(1), 490–9.

Liu, F., Chen, G., Li, L., Guo, Y., 2012. Study impact performance of rubber reinforced concrete, Construct Build Mater. 36, 604-616.

Mansur, M.A., Ahmad, I., Paramasivam, P., 2001. Punching shear failure of simply supported ferrocement slabs. J. Mater. Civ. Eng. 13(6), 418-426

Naaman, A.E., 1979. Design predictions of crack widths in ferrocement. Ferrocement–Materials and applications. Detroit: American Concrete Institute. 19, 25–37.

Naaman, A.E., 2000. Ferrocement and laminated cementitious composites. Ann Arbor, Michigan: Techno Press 3000.p. 372.

NDIS 2421 (2000), Recommended Practice for In-Situ Monitoring of Concrete Structures by Acoustic Emission, Japanese Society for Non-Destructive Inspection.

Oikonomou, N., Mavridou, S., 2009. Improvement of chloride ion penetration resistance in cement mortars modified with rubber from worn automobile tires. Cem Concr Compos. 31(6), 403–407

Onuaguluchi, O., Panesar. D.K., 2014. Hardened properties of concrete mixtures containing pre-coated crumb rubber and silica fume. . J Clean Prod. 82, 125-131.

Paul, B.K., Rama, R.P., 1978. Ferrocement. Bangkok: International Ferrocement Information Center. p. 179.

Ranjbar, R., Behnia, A., Alsubari,Birgani, P.M., Jumaat, M.Z. 2016a. Durability and mechanical properties of self-compacting concrete incorporating palm oil fuel ash. . J Clean Prod. 112, 723-730.

Ranjbar, N., Mehrali, M,.Behnia, A., Alengaram, U.J., Jumaat, M.Z., 2014. Compressive strength and microstructural analysis of fly ash/palm oil fuel ash based geopolymer mortar. Mater Design. 59, 532-539.

Ranjbar, N., Mehrali, M., Behnia, A., Pordsari, A.J., Mehrali, M., Alengaram, .U.J. 2016b, A Comprehensive Study of the Polypropylene Fiber Reinforced Fly Ash Based Geopolymer. PloS one, 11(1), e0147546.

Ranjbar, N., Talebian, S., Mehrali, M., HendrikC.K., Jumaat, M.Z. 2016c. Mechanisms of interfacial bond in steel and polypropylene fiber reinforced geopolymer composites. Composites Science and Technology. 122, 73-81.

RILEM TC 212-ACD, 2010. Acoustic emission and related NDE techniques for crack detection and damage evaluation in concrete. Mater Struct. 43, 1183-1186.

Shah, S.P., Li, Z., 1994. Localization of micro cracking in concrete under uniaxial tension. ACI Mater J. 91(4), 372–81.

Shiotani, T., Aggelis, D.G., 2007. Evaluation of repair effect for deteriorated concrete piers of intake dam using AE activity. Journal of Acoustic Emission. 25, 69–79.

Shiotani, T., Fujii, K., Aoki, T., Amou, K., 1994. Evaluation of progressive failure using AE sources and improved B-value on slope model tests. Prog Acoust Emiss. 7, 529–34.

Soulioti, D., Barkoula, N.M., Paipetis, A., Matikas, T.E., Shiotani, S., Aggelis, D.G., 2009. Acoustic emission behavior of steel fibre reinforced concrete under bending Construct Build Mater. 23, 3532-3536.

Su, H.,Yang, J., Ling, T.C.,Ghataora, G.S., Dirar, S., 2015. Properties of concrete prepared with waste tyre rubber particles of uniform and varying sizes. J Clean Prod. 91, 288-296.

Svec, O., Ziregulis, G., Bolander, J.E., Stang, H., 2014. Influence of formwork surface on the orientation of steel fibres within self-compacting concrete and on the mechanical properties of cast structural elements. Cem Concr Compos. 50, 60-72.

Topçu, I., Bilir, T., 2009. Experimental investigation of some fresh and hardened properties of rubberized self-compacting concrete. Mater Design. 30, 3056-3065.

Yerramala, A., Ramachandurdu, C., Desai, B., 2013. Flexural strength of metakaolin ferrocement. Composites: Part B. 55, 176–183.
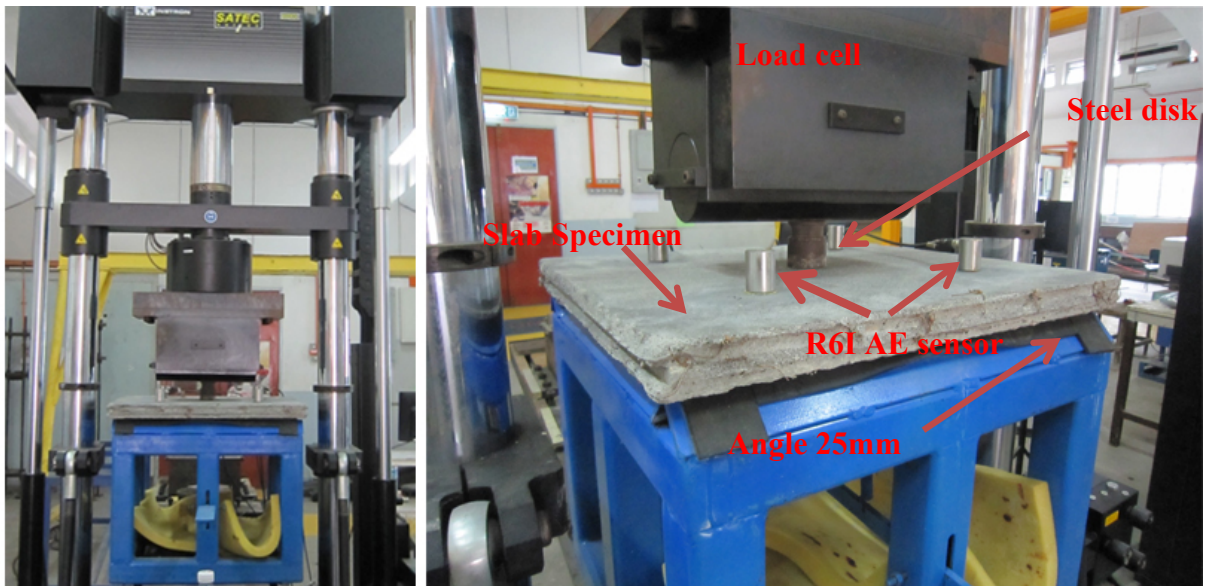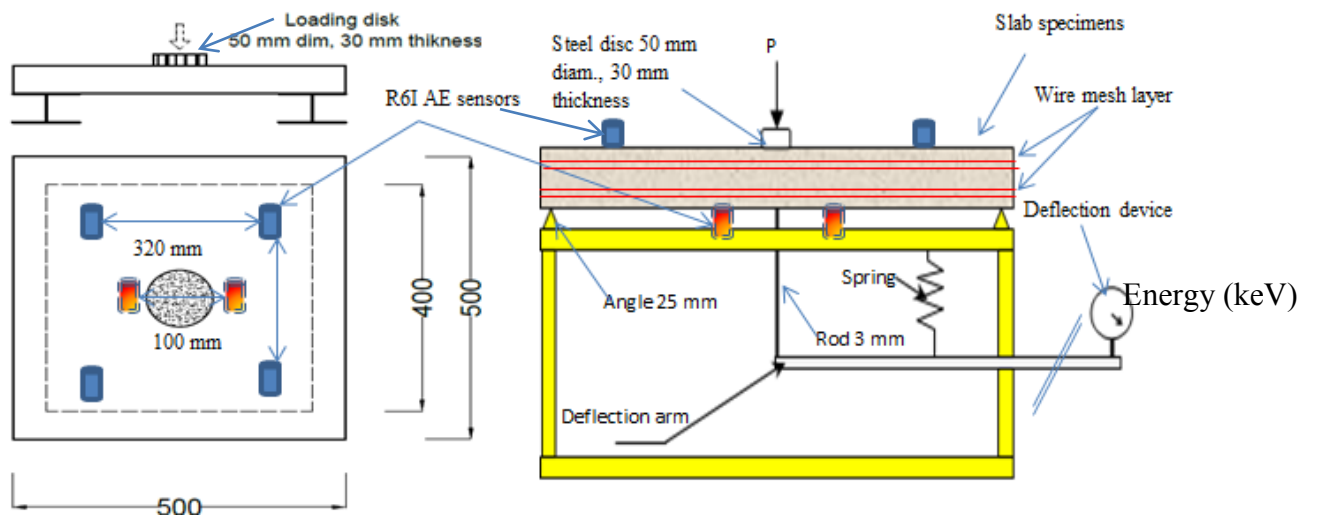
Figure.1: Test setup and flexural strength test of ferrocement slab and AE sensor placement
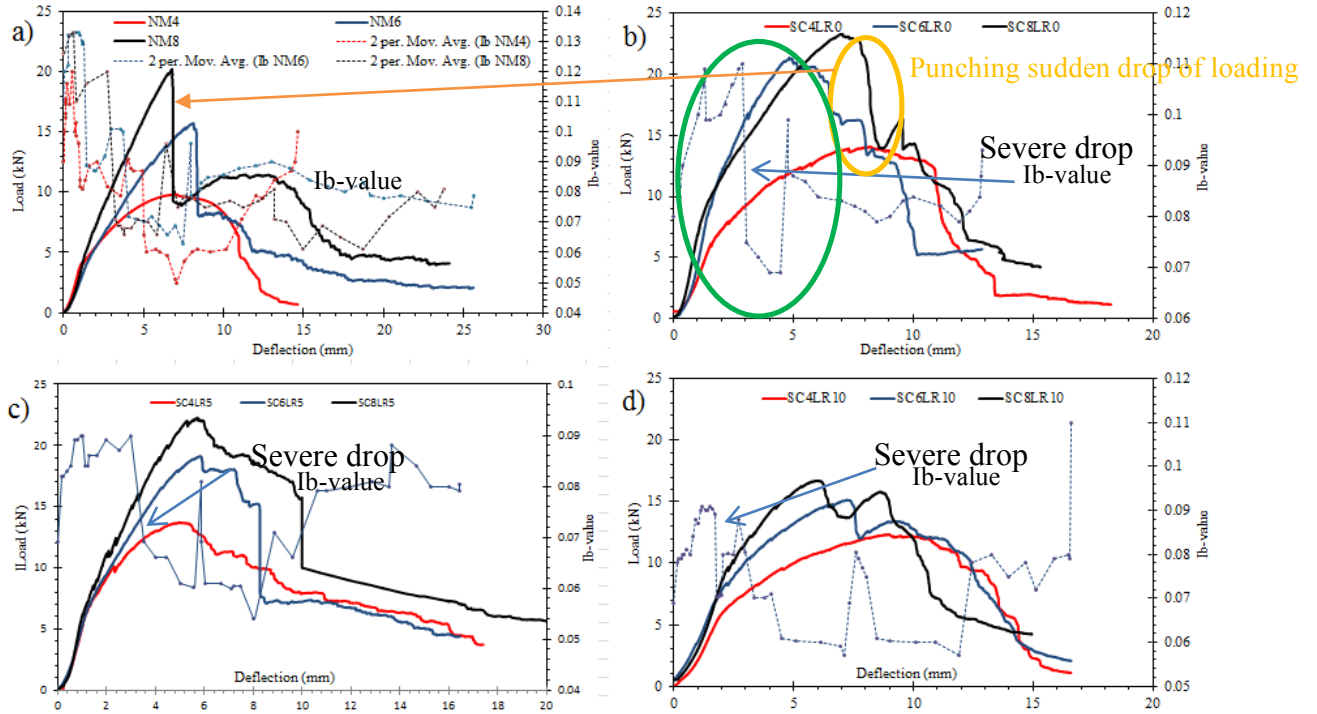
Figure.2 Load- deflection curves and Ib-value for ferrocement slab specimens: a) Normal mortar series (NM), b) Self-compact mortar series (SCMR0), c) Self-compact 5% rubberized mortar series (SCMR5), d) Self-compact 10% rubberized mortar series (SCMR10)
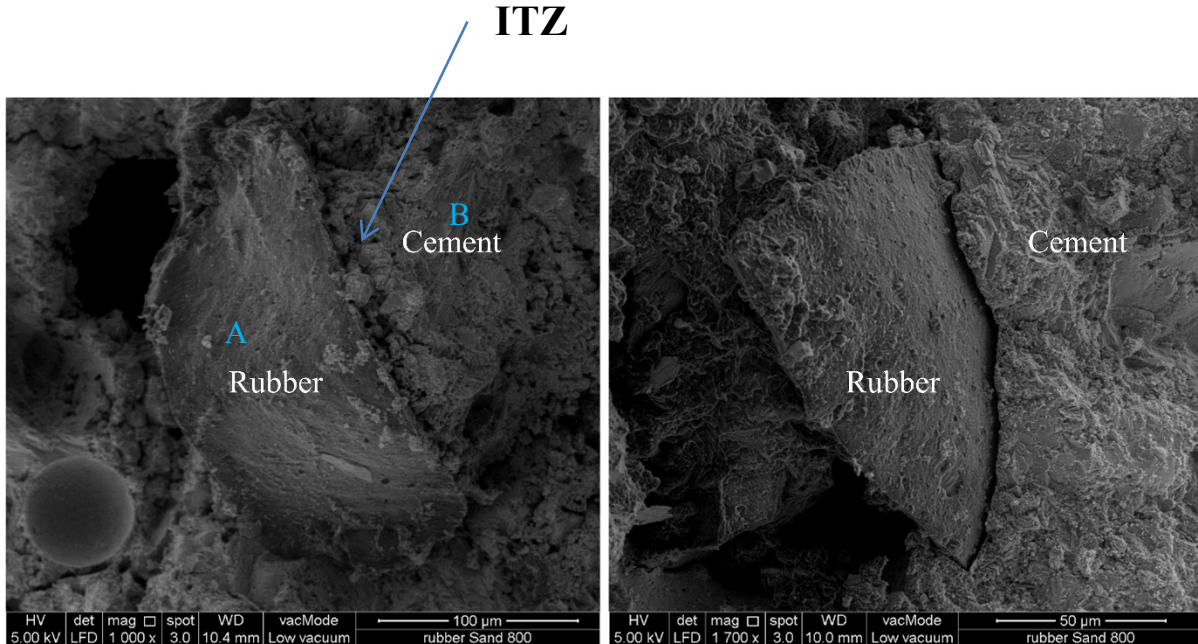

Figure.3: SEM images of interfacial bond of rubber particles and cement paste (A) Rubber particle; (B) Cement paste.
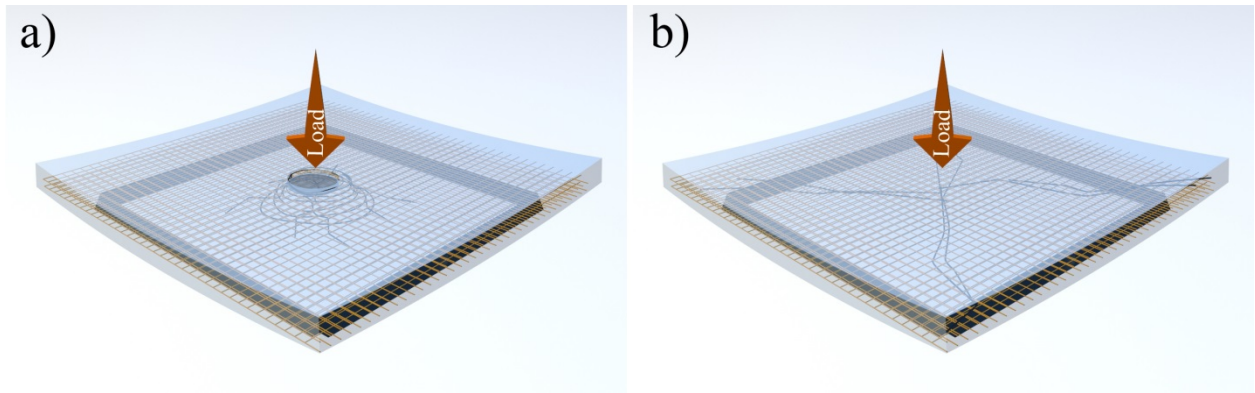
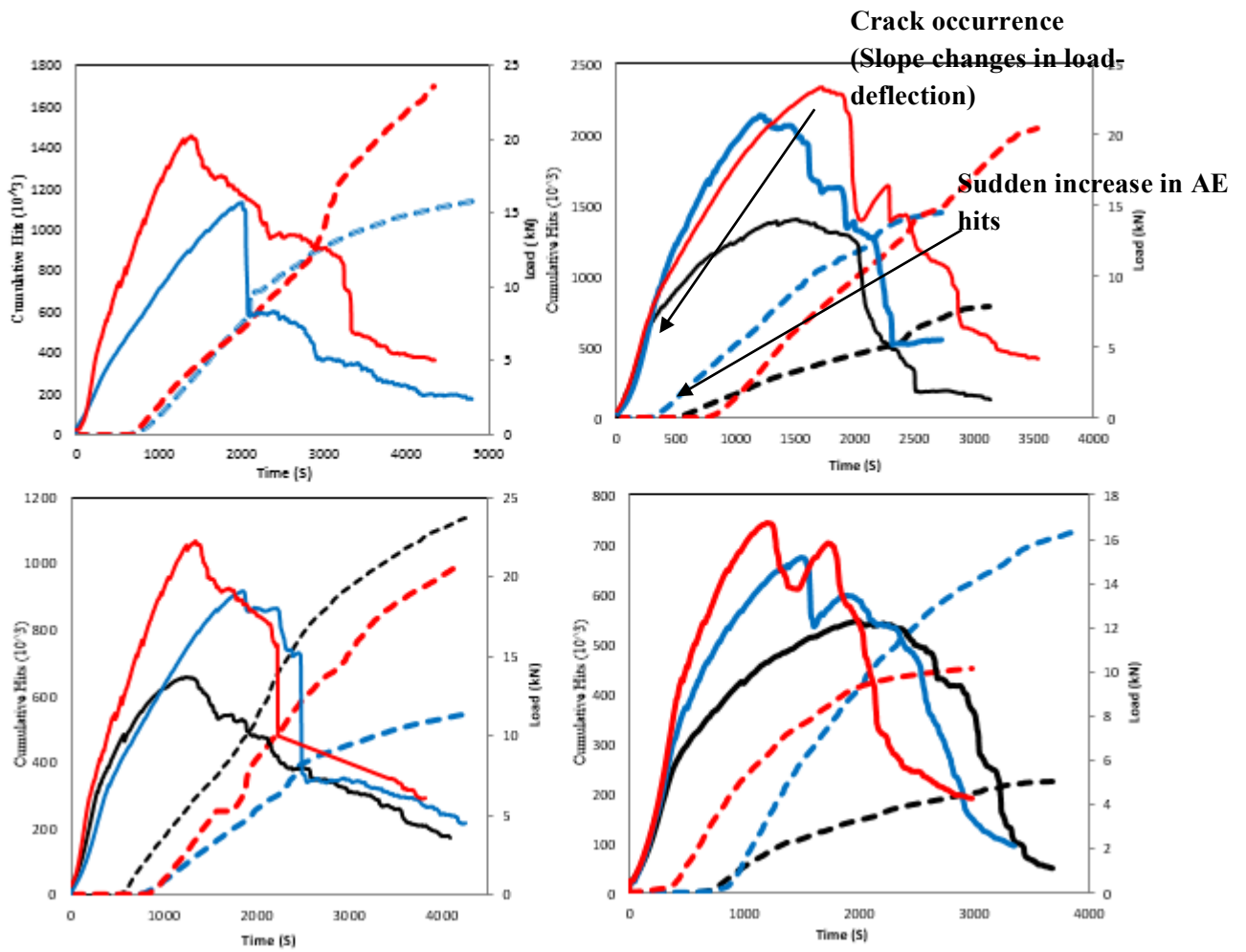Figure.4: Schematic of failure modes: a) Punching failure, b) Flexural failure

Figure.5: Cumulative AE hits for all sensors, a) Normal mortar, b) SCM, c) SCMR5, d) SCMR10 (All sensors) —— 4 layers —— 6 layers —— 8 layers (Loading)

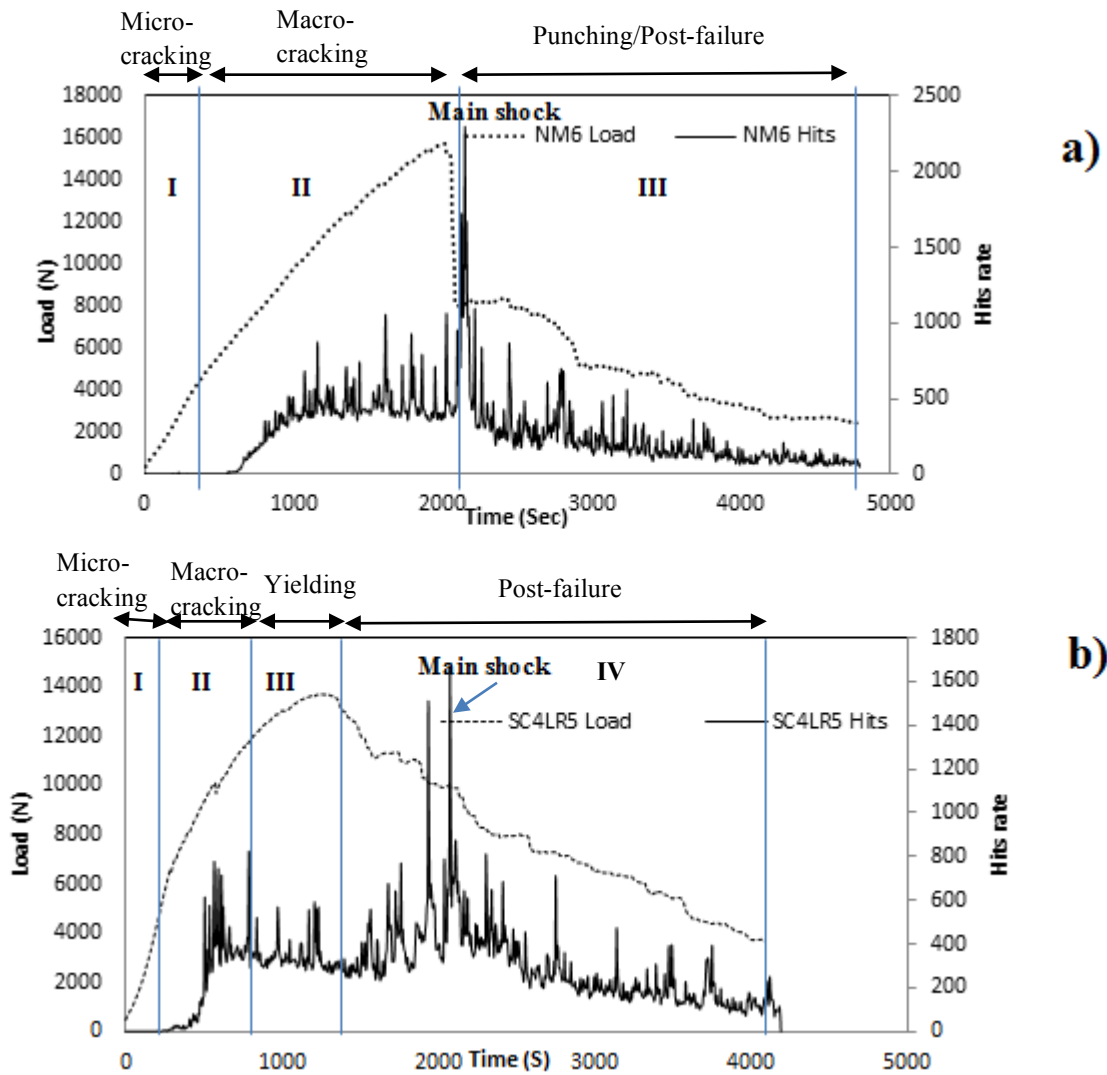········ 8 layers ········ 6 layers ········ 8 layers (Hits)

Figure.6: Typical example of AE hits rate against loading for: a) Punching failure, b) Flexural failure
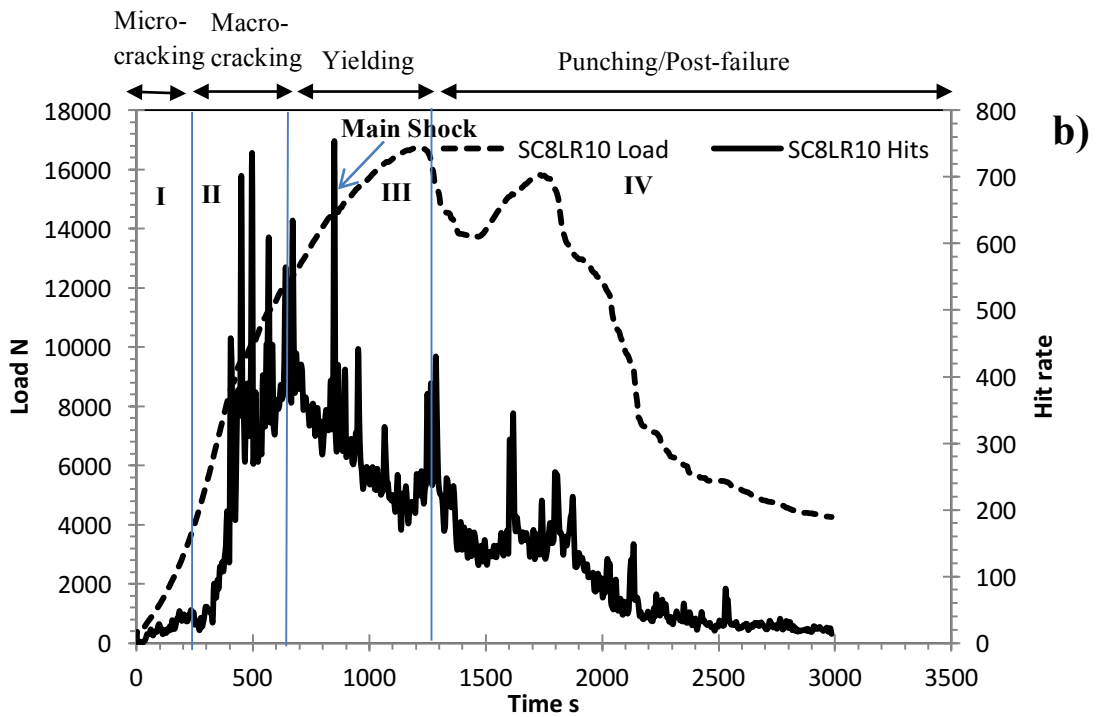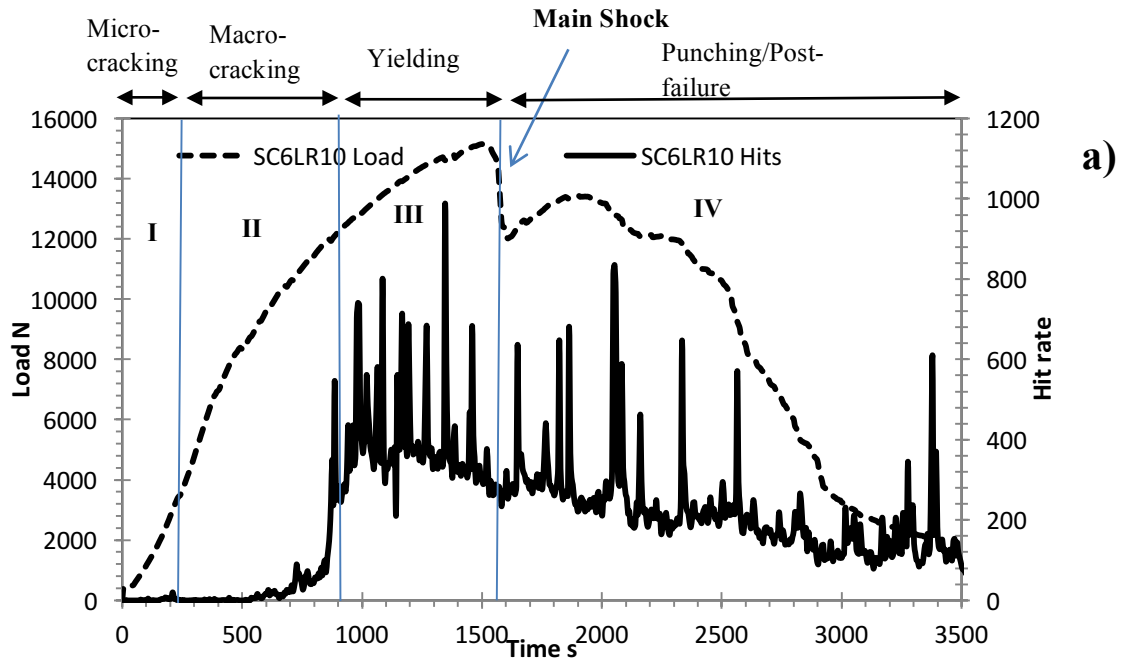
Figure.7: Typical example of AE hit rates against loading for sample with maximum rubber: a) SC6LR10, b) SC8LR10

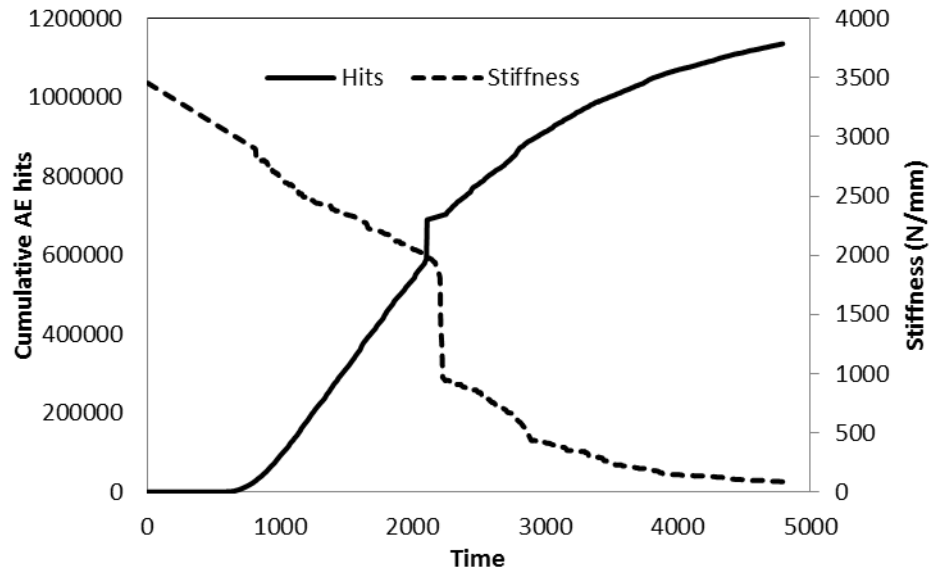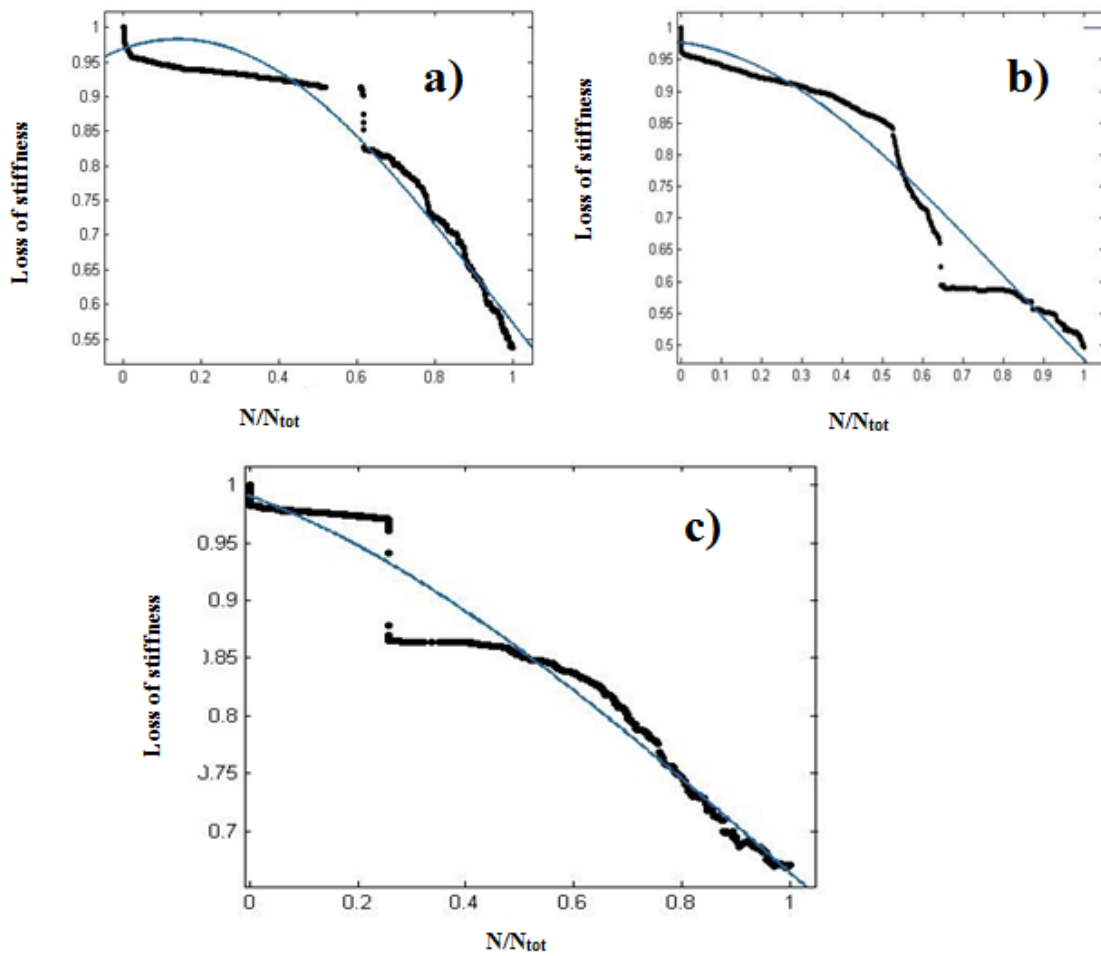Figure.8: Cumulative AE hits and stiffness versus time for NM6

Figure.9: Loss of stiffness versus normalized cumulated AE hits, a) NM6, b) SC4LR0, c) SC8LR5
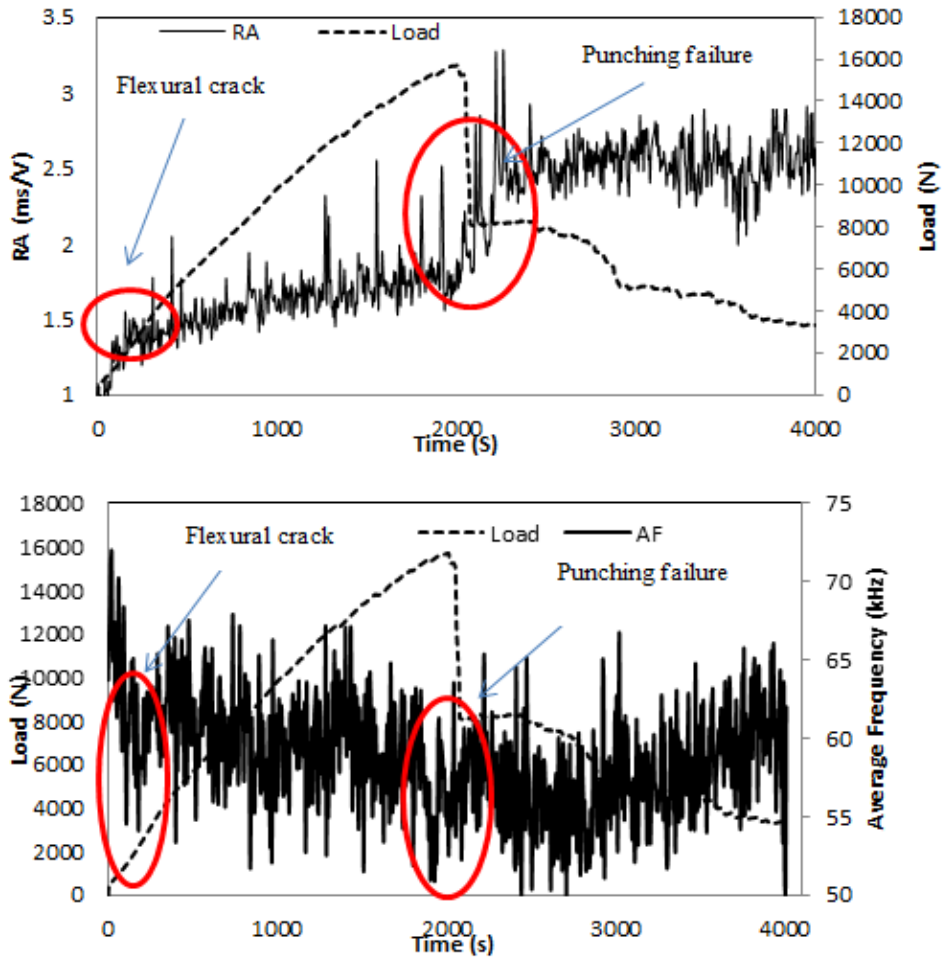
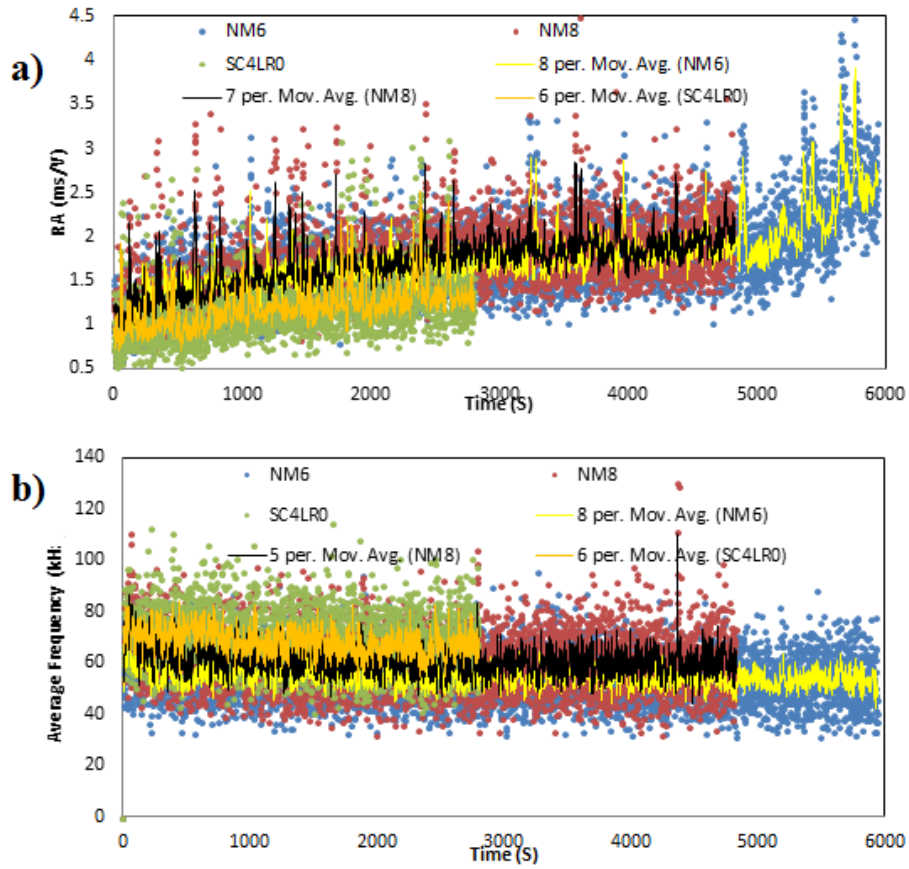Figure.10: RA and Average frequency variation against loading for NM6

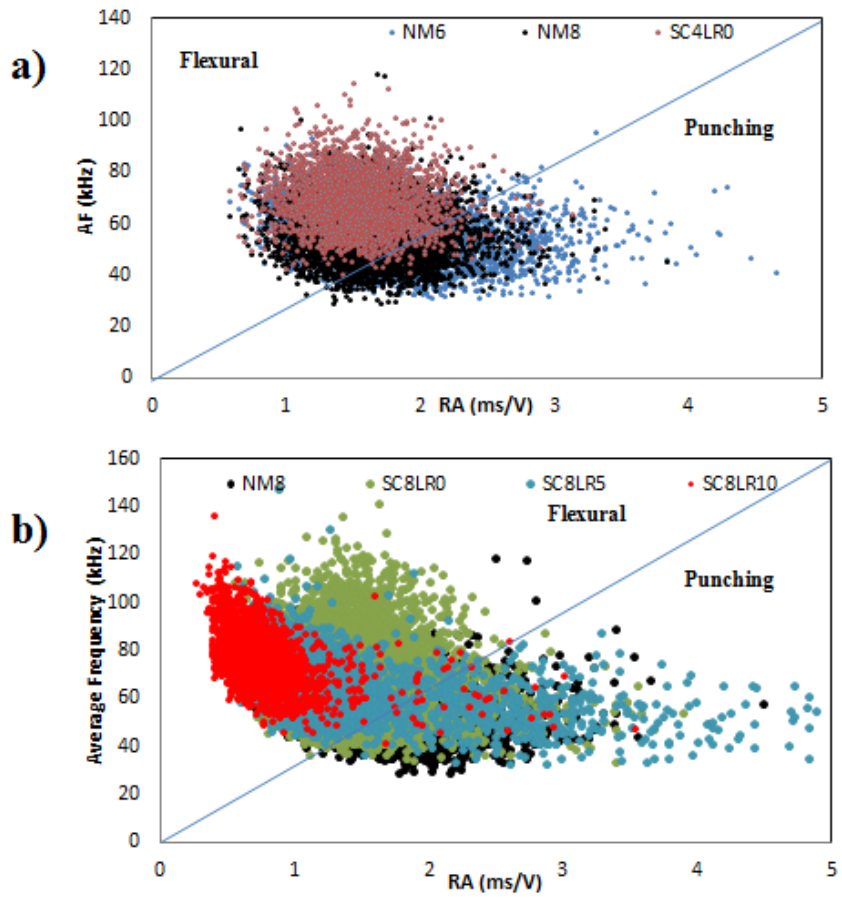Figure.11: Trend of variation of AE features in different type of failures: a) RA, b) AF

Figure.12: Failure type classification based on average frequency versus RA

Table 1

Chemical composition and physical properties of FA

Composition	FA%
SiO_2	54.715
K_2O	1.003
Fe_2O_3	5.149
CaO	5.306
P_2O_5	1.115
MgO	1.103
Al_2O_3	27.280
SO_3	1.008
TiO_3	1.817
Na_2O	0.434
MnO	0.099
CuO	0.010
Rb_2O	0.007
ZnO	0.031
Cr_2O_3	0.042
SrO	0.361
NiO	0.022
ZrO_2	0.162
Y_2O_3	0.017
LO_1	6.800

Median particle size(μm)	Specific gravity (gr/cm^3)	BET (m^2/g)
16.23	2.18	2.96

Table 2

Proportion of constituent materials and rheological properties of mortar mixes and slabs

Series	Cement	Sand	Fly ash(FA)	Super plasticizer (% of cement)	Rubber Powder	Wire Mesh Layers	Specific surface cm^2/cm^3	Number of specimens
NM4	1	1.5	0	0	0	4	0.7112	1
NM6	1	1.5	0	0	0	6	1.0668	1
NM8	1	1.5	0	0	0	8	1.4224	1
SCL4R0	1	1.5	20%	1%	0	6	0.7112	2
SCL6R0	1	1.5	20%	1%	0	6	1.0668	2
SCL8R0	1	1.5	20%	1%	0	8	1.4224	2
SCL4R5	1	1.5	20%	1.1%	5%	4	0.7112	2
SCL6R5	1	1.5	20%	1.1%	5%	6	1.0668	2
SCL8R5	1	1.5	20%	1.1%	5%	8	1.4224	2
SCL4R10	1	1.5	20%	1.5%	10%	4	0.7112	2
SCL6R10	1	1.5	20%	1.5%	10%	6	1.0668	2
SCL8R10	1	1.5	20%	1.5%	10%	8	1.4224	2

SCM mortar: Self-compacted mortar

RSCM mortar: Rubberize self-compacted mortar

Table 3
Chemical composition and physical properties of tire rubber

Specification	Test Method	Content (%)	Specification (%)
Acetone Extract	ISO 1407	9.3	10±3
Ash Content	ASTM D6370-99	8.5	8±3
Carbon Black	ASTM D6370-99	28.1	30±5
Rubber Hydrocarbon	ASTM D6370-99	50.2	52±5
Heat Loss	ASTM D1509	0.9	< 1%
Metal Content	ASTM D5603	0.8	< 1%
Fiber Content	ASTM D5603	1.5	< 2%

Table 4
Fresh and hardened properties of mortar

Series	Slump flow (mm)	mini J-ring (mm)	mini V funnel (Sec)	Comp.@ 7day (Mpa)	Comp.@ 28day (Mpa)	Tensile (Mpa)
NM	-	-	-	31.2	44.4	8.16
SCMR0	285	280	9.72	41.5	59.2	12.03
SCMR5	260	240	10.19	39.4	55.7	10.27
SCMR7	245	230	14.03	37.2	51.9	9.95
SCCM10	230	225	18.78	33.7	48.5	9.72

Table 5

Test results for ultimate load, flexural strength, ultimate deflection and fracture mode

Meshing layers	Slab	Load at failure (N)	Flexural strength (N/mm²)	Deflection at failure (mm)	Energy absorption at failure (N.mm)	Ultimate Energy absorption (N.mm)	Ductility ratio (D_r)	Mode of fracture
4	NM4	9650.42	23.161008	6.89	52500	89625	3.56	Flexural failure
	SCL4R0	14067.5	33.762048	8.01	75600	133600	4.4	Flexural failure- rupture of mesh
	SCL4R5	13718.9	32.925456	5.01	55600	130400	4.65	Flexural failure/ Rupture of mesh (failure started by slight punching but followed but flexural)
	SCL4R10	12353.2	29.647728	10.07	141200	289000	5.92	Full flexural failure- starting from center at the bottom- fully two ways action- high ductility- yield of mesh- divided to four equal square- stress distribution was full event.
6	NM6	15732.4	37.757736	7.97	81000	144875	3.03	Punching failure/Fracture of mesh/ debonding between concrete and meshing
	SCL6R0	21394.3	51.3462	4.8	66800	154800	3.51	Flexural semi-Punching failure- Rupture of mesh
	SCL6R5	19147.8	45.954696	5.7	71200	159200	4.79	Punching - started by flexural failure but dominated by punching- nearly one way yield of mesh- top surface only faced a punch by load surface and cracks did not extend to the top surface, meaning punch dominated
	SCL6R10	15149.2	36.358184	9.5	80400	158400	5.3	Flexural failure/ fully two ways action/ high ductility/ yield of mesh/ Stress distribution was full (Bridging effect)
8	NM8	20254.97	48.611928	6.5	87500	183000	3.6	Punching started by flexural fracture/Fracture of mesh
	SCL8R0	23318.24	55.963776	6.8	101600	187200	5.5	Starting with flexural cracks but fails in punching mode/rupture of mesh
	SCL8R5	22045.64	52.909536	6.9	88800	209000	5.61	Punching- top surface not affected/ after punching on the bottom surface, wires started to deform by concrete till rupture
	SCL8R10	16722.74	40.13458594	8.5	176400	384400	5.71	Flexural failure/ fully two ways action/high ductility/yield of mesh/ Stress distribution was full event (Bridging effect)

Table 6
Gaussian model confidence level and parameters

Sample	a_1	b_1	c_1	R-square	SEE	RMSE
NM4	0.98	0.14	1.17	0.9725	0.63225	0.02602
SC4LR0	0.98	0.06	1.2	0.9593	0.7044	0.03404
SC8LR5	1.02	0.04	2.1	0.9721	0.3007	0.01938